Insights into dike nucleation and eruption dynamics from high-resolution seismic imaging of magmatic system at the East Pacific Rise

Milena Marjanović, Suzanne Carbotte, Alexandre Stopin, Satish Singh, René-Édouard Plessix, Miloš Marjanović, Mladen Nedimović, Juan Pablo Canales, Hélène Carton, John Mutter, et al.

GEOPHYSICS

Insights into dike nucleation and eruption dynamics from high-resolution seismic imaging of magmatic system at the East Pacific Rise

Milena Marjanović[1]*, Suzanne M. Carbotte[2], Alexandre Stopin[3]†, Satish C. Singh[1], René-Édouard Plessix[3], Miloš Marjanović[4], Mladen R. Nedimović[2,5], Juan Pablo Canales[6], Hélène D. Carton[1,2], John C. Mutter[2], Javier Escartín[7]

Models of magmatic systems suggest that the architecture of crustal magma bodies plays an important role in where volcanic eruptions occur, but detailed field observations are needed to evaluate them. We present ultra-high-resolution reflection images of magma bodies beneath a region of multiple eruptions along the East Pacific Rise derived from three-dimensional seismic surveying. The observations reveal magma bodies with elongate ridges and troughs vertically aligned with seafloor eruptive fissures that we interpret as remnant dike root zones where repeat dikes nucleate. We document a triangular feeder zone to the axially centered magma body from the off-axis source for a newly forming seamount of the Lamont chain and infer bottom-up eruption triggering due to recharge from this deeper source. The findings indicate that magma bodies are sculpted by both processes of magma recharge from below and magma extraction to the surface, leaving a morphological imprint that contributes to localization of dike nucleation and eruption sites at the East Pacific Rise.

INTRODUCTION

The architecture of magma plumbing systems and how magmas move through them play a fundamental role in volcano construction and evolution (*1*–*4*). The plumbing system includes conduits via which magma is transported through the crust and magma bodies where magma is stored (*1*, *4*–*7*). Magma ascent is governed by the range of stresses acting within and upon the system, including magma pressure and regional tectonic and gravitational stresses, and strong feedbacks between the architecture of the plumbing network and volcano stress field are expected [e.g., (*1*, *4*)]. Growing observations from diverse volcanoes formed in different tectonic settings show evidence for local magma accumulations concentrated at multiple levels in the crust with magma transport between them taking place via intrusion and/or processes of buoyant porous flow [e.g., (*2*–*3*, *8*)]. Magma propagation to the surface leading to volcanic eruptions is primarily governed by processes within the shallow part of the system with conduits, including dikes, nucleating from and tapping the shallow-level magma bodies (*4*, *9*, *10*). Where and how dikes nucleate from shallow magma accumulations to breach the layer above and erupt and how magma bodies drain during eruptions are subjects of ongoing debate and are of central importance for volcano hazard assessment. One of the commonly assumed conceptual models of conduit formation invokes "bottom-up" processes whereby magmatic overpressures developing in upper crust magma accumulations exceed the tensile strength of the host rock leading to dike nucleation and rupture to the surface [e.g., (*11*–*13*)]. An alternative model suggests "top-down" processes by which tectonic extension, cracking, volcano unloading by, for example, lava-dome collapse, and degassing above the magma reservoir lead to conduit opening and magma ascent [e.g., (*14*–*20*)]. Obtaining a detailed architecture of the shallow magma accumulations is important for evaluating end-member models and for understanding what controls the location, style, frequency, and duration of volcanic eruptions. However, because of the general inaccessibility of active volcanic systems to high-resolution imaging, the detailed morphology of the shallowest melt accumulations from which volcanic eruptions are staged is largely unknown, and relationships to dike nucleation and eruption dynamics are poorly understood.

Mid-ocean ridges (MORs), which are the most extensive magmatic systems on Earth (*21*), can be readily scanned by controlled-source marine seismic techniques to resolve the structure and characteristics of the magma plumbing system, with the shallowest regions accessible to much higher-resolution imaging than is possible in subaerial settings. At fast-spreading ridges, elongate quasi-linear axial magma lenses (AMLs) are found ubiquitously (*11*, *22*–*27*), representing upper crustal magma accumulations at the top of a broader transcrustal zone of mush and melt (Fig. 1) (*28*, *29*). The AML forms at the interface between the brittle upper crustal lid and the magmatic ductile regime of viscous flow below, where elastic stresses rapidly dissipate. Dike root zones (DRZs) develop within this boundary region, nucleating at and connecting to magma source accumulations (*13*).

One of the best-studied portions of the MOR system is the East Pacific Rise (EPR) centered at latitude 9°50′N (Fig. 2A). It is renowned for prolific hydrothermal venting [e.g., (*30*, *31*)] and recurrent volcanic eruptions. The first documented eruption occurred in 1991/1992, and the second possibly initiated in early 2005, with the

[1]Institut de Physique du Globe de Paris, Université Paris Cité, CNRS UMR7154, Paris, France. [2]Department of Marine Geology and Geophysics, Lamont-Doherty Earth Observatory, Columbia University, Palisades, NY, USA. [3]Shell Global Solutions International B.V., Amsterdam, Netherlands. [4]Faculty of Mining and Geology, University of Belgrade, Belgrade, Serbia. [5]Department of Earth and Environmental Sciences, Dalhousie University, Halifax, Nova Scotia, Canada. [6]Department of Geology and Geophysics, Woods Hole Oceanographic Institution, Woods Hole, MA, USA. [7]Laboratoire de Géologie, École Normale Supérieure (CNRS UMR), PSL Research University, Paris, France.
*Corresponding author. Email: marjanovic@ipgp.fr
†Present address: Bureau de Recherches Géologiques et Minières (BRGM), Orléans, France.

primary eruption episode in January 2006 (*14*, *32*, *33*). The seafloor geology of the site of the most recent eruption, which extends from ~9°48′ to 9°56′N, is now known on meter scales and in three dimensions. The resulting mapping includes the detailed distribution and morphology of the erupted lavas (*34*–*37*), their geochemical variations (*38*), and the geometry of the axial eruptive fissure zone embedded in a broader (on average, 60 to 70 m wide) axial summit trough (AST; Fig. 2A) (*34*–*36*). On the basis of these high-resolution observations, the AST is believed to be the long-term locus of eruptions.

In Summer 2008, a three-dimensional (3D), multistreamer and multichannel seismic survey was conducted focusing on the EPR 9° 50′N eruption site (*39*–*42*) (Materials and Methods; fig. S1). The collected data has brought a wealth of information regarding the magmatic system. The along-axis swath images of the 8- to 120-m-thick (*43*) magma lenses, displaying variable melt content (*44*), showed fine-scale partitioning of the magmatic system (5 to 15 km) and its genetic relationship with seafloor tectonic segmentation (*23*, *40*). The same dataset allowed for high-resolution imaging of deeper portions of the axial magma chamber for the first time and led to the discovery of magma accumulations at multiple levels (*22*) immersed in a mushy mid-crust (Fig. 1) with vertically stacked lenses potentially contributing to single volcanic eruption episodes (*11*, *22*). The seismic volume collected during the same expedition (fig. S1) also revealed networks of lower-crustal magma accumulations outside the axial accretion zone (*41*, *42*, *45*), providing magma reservoirs for off-axis eruptions where magmas from distinct upper mantle sources may mix (*41*).

While much has been learned from these prior studies, the shallowest part of the magmatic system beneath the ridge axis region (AML) has not been previously explored in three dimensions. To close the large resolution gap and allow for direct comparisons of the structural characteristics of the AML with the eruptive products of the last eruption, we processed the seismic volume collected in 2008 using advanced seismic techniques (Materials and Methods). State-of-the-art elastic full-waveform inversion (FWI; inverting for both *P*- and *S*-waves) (*46*) was used to derive the best constrained 3D velocity (Vp) model of the upper crust in the study region (*39*), which was then used to carry out 3D prestack depth migration scheme on a high-resolution grid 25 m by 25 m by 5 m (Materials and Methods; fig. S1). The results provide unique 3D images of the shallow magma lenses beneath the site of recurrent eruptions at an unprecedented resolution (Figs. 2 and 3 and fig. S2). The only other study in which FWI-derived Vp models have been used to image the shallow magma system made use a limited suite of 2D seismic profiles (Axial Volcano, Juan de Fuca Ridge) (*11*, *47*). However, because of the inherent limitation of 2D imaging and techniques applied (both FWI and migration) and the limited dataset available, only large-scale structural variations were interpretable.

RESULTS

The 3D images of the EPR magmatic system reveal a complex network of crustal magma bodies from ~9°47′ to 9°56′N with notable morphological and structural variations that can be best appreciated in the mapped seismic horizons (Fig. 2B and fig. S2). Although the seismic horizon depicting the main AML appears as a continuous feature, three morphologically distinct magmatic units can be defined on the basis of their depth, orientation, and geometry. The latitudinal extents of these units correspond to the fine-scale tectonomagmatic segments previously identified as physically separated lenses that erupt distinct lava compositions (*23*, *38*), which we identify as the southern (9°47′ to 9°48.8′N), central (9° 48.8 to 9°51.4′N), and northern (9°51.4′ -9°56.5′N) magmatic segments (Figs. 2B and 3 and fig. S2). In the following, we describe the architecture of each magmatic segment and linkages with seafloor eruption characteristics. Map-view images and representative seismic profiles are shown for each segment in Figs. 4 to 6, and summary schematic profiles illustrating our interpretations of the main features of the magmatic system in each segment are shown in Fig. 7.

Southern magmatic segment

The southern segment erupted the smallest-volume lava flow during the last documented eruption, which overtopped the ~100-m-wide AST and flowed up to 1.2 km down the ridge flanks north of 9°47′N (Fig. 4A) (*34*, *35*). In the underlying subsurface, the 3D seismic images reveal a complex magma body up to 1.7 km wide with different characteristics coincident with the seafloor transition at 9°47′N, demarked by an offset (<100 m) in the AST (fig. S3, A and B). Beneath the ridge axis, the top of the magma accumulation is characterized by a narrow (<200 m wide) and ~100-m high ridge-like structure. This AML ridge extends for most of the length of this segment and is vertically aligned with the narrower AST above (Fig. 4A and figs. S3, A and B, and S4A). In the morphology of the AML south of 9°47′N, another ridge-like feature, parallel and shifted ~400 m to the west from the axis-centered one, is present. Most of the hydrothermal vents associated with the southern magmatic segment are found along this southernmost portion, which did not erupt in 2005–2006. North of 9°47′N, the cross-axis depth of the AML is highly asymmetric, with the western wing down-dropped for >150 m with respect to the axis-centered feature (Fig. 4). Around 9°48′N and further to the north, the complexity in the AML reflector [average depth, 1440 m below seafloor (bsf)] suggests two overlapping magma bodies extending parallel to each other (Fig. 4). Within the region of cross-axis AML asymmetry, a separate shallower lens lies beneath the eastern flank at ~1250 m from the axis (Fig. 4A and fig. S4, A and B). This unusual upper-crustal off-axis magma lens (uOAML) is ~3.5 km long and <1 km wide and spans depths from ~3100 to 3700 m below sea surface (530 and 1100 m bsf, respectively), which locates it within the dike section (Figs. 4A and 7A and fig. S4D). The presence of localized steeply dipping reflectors (43°) from the western edge toward the AML (Materials and Methods) indicates that this uOAML is fed via channels from the axis (Figs. 4B and 7A). Spatial correlation between this shallow magma lens (uOAML) and magma lenses previously identified in the lower crust (OAMLs) (*42*) and a melt anomaly identified from seafloor compliance studies (*48*) suggest that this magma body is also supplied from the deeper crust below. On the basis of the energy attribute, used as proxy for relative variation of melt versus crystal content from the recorded amplitudes in seismic signal (Materials and Methods), the latter view is further supported by the presence of higher seismic amplitudes (i.e., potentially higher melt content) that characterizes the uOAML within the same region (fig. S4B). The eastern edge of the uOAML underlies and follows the strike of an obliquely trending off-axis fault (*37*) and volcanic ridge at the seafloor (Fig. 2A and

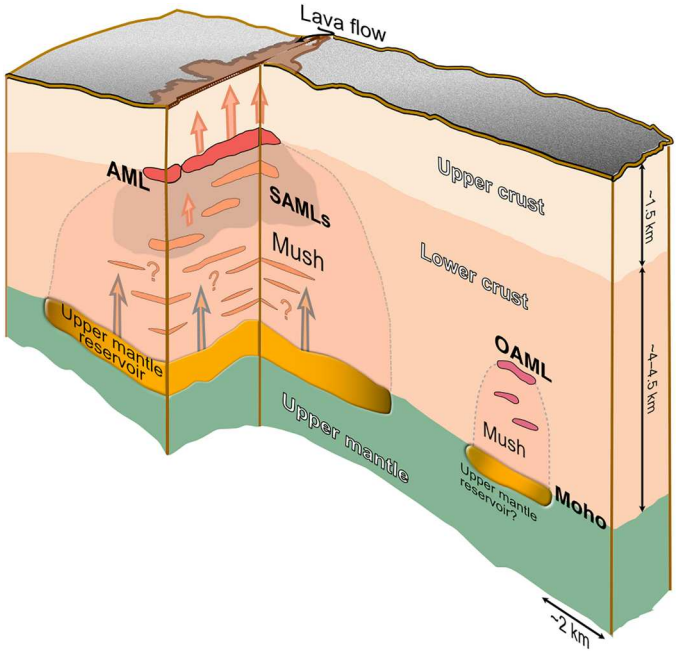

Fig. 1. Schematic illustration of the magmatic system at the EPR 9°50′N. The axial magma chamber is represented by the topmost AML and mid-crustal sub-AMLs (SAMLs) embedded in a broader zone of mush (*22*, *23*, *28*, *29*). The potential presence of deeper, thinner SAMLs in the lower crust is indicated with question marks, as their presence is inferred primarily from ophiolite exposures. The mid-crustal SAMLs are encompassed by a mushy region, marked with the gray-shaded zone representing mush with a higher percentage of melt (*11*, *29*). At the base of the crust, a broader ~10-km-wide zone of accumulating melt in the uppermost mantle is inferred from low *P*-wave velocities in seismic tomography studies (dark yellow) (*55*). Away from the ridge axis, lower crustal off-axis magma lenses (OAMLs) are present (*41*, *42*, *45*). They are encompassed by an inferred higher-temperature mushy region and underlain by a potential upper mantle reservoir. Moho indicates the Mohorovičić discontinuity. The illustration is not drawn to scale; we provide approximative vertical and horizontal scales for the upper and lower crust as guidance. The presented magma bodies are highly vertically exaggerated.

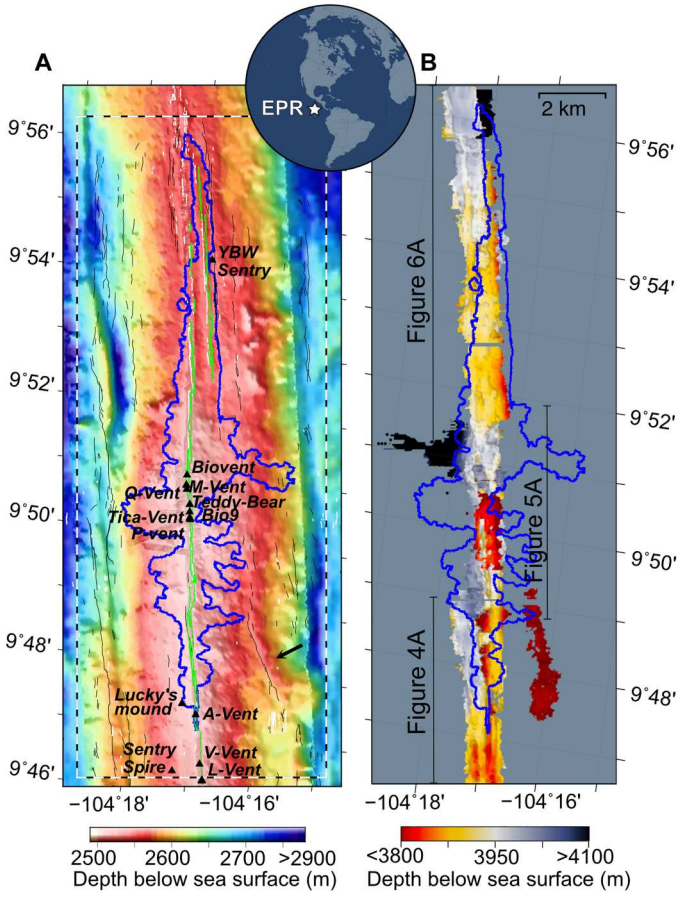

Fig. 2. Regional seafloor tectonics and 3D morphology of the magma body at the EPR 9°50′N. (**A**) Seafloor bathymetry, combining grids sampled at 3 m (*70*), 30 m (*71*), and 50 m (collected during the 2008 survey), shows the location of morphotectonic elements of the ridge crest zone: hydrothermal vents in black triangles (*31*), 2005–2006 lava flow in blue, faults in black, fissures in white, and AST in green lines (*35*–*37*). The black arrow points to the obliquely trending volcanic ridge ~9°48′N. The black-white dashed box outlines the region shown in (B). The inset globe indicates the location of the EPR study area. (**B**) Plan view of the AML with the extent of the southern, central, and northern AML segments marked and also shown in Figs. 4A, 5A, and 6A. The same panel without interpretation is shown in fig. S2A.

fig. S3B), indicating a long-term history of volcanic eruptions from this body.

Central magmatic segment

The central segment (Fig. 5) is considered the initiation site of the last documented eruption and the long-term persistent locus of eruptions based on the locally shallower seafloor topography (*14*, *32*, *35*). It is also the location of the highest–effusion rate and largest-volume lava flows, highest-temperature magmas based on high MgO (wt %) compositions, and many high-temperature vent sites (fig. S5) (*30*, *31*). The AML underlying this region is narrower (average width, ~1 km) and deeper than in the adjoining segments to the south and north (1515 m versus 1440 m and 1390 m bsf, respectively; Figs. 2B and 3). The deepest patch of this AML segment is its northernmost part where a triangular sheet or channel (width varying from 225 to 1625 m) is imaged, plunging from the main magma body at an 8.5° dip (deepening by ~450 to 500 m on average) to the west (Fig. 5A). The farthest and narrowest part of this triangular sheet reaches 2.5 km from the ridge axis, ending at the subsurface projection of a prominent axis-facing fault, with an offset of ~200 m at the seafloor (Fig. 8).

South of 9°51′N, the morphology of this AML segment is dominated by a trough-like structure (~40 to 60 m deep), extending for ~3.7 km along the ridge axis (Fig. 5A and fig. S6, A and B). For most of its length, the trough is ~200 m wide, runs parallel to the AST, and is bounded by shallower, ridge-like features. At ~9°50.6′N, these ridges disappear, and the trough changes orientation in a 20° counterclockwise rotation, trending obliquely to the AST and toward the westwardly dipping triangular channel for another 650 m; it also widens and deepens to ~350 and 85 m, respectively. Along most of its extent, the trough is characterized by low values of the energy attribute (fig. S7; Materials and Methods), suggesting the presence of highly crystallized magma. Furthermore, the obliquely trending trough underlies the deepest portion of the AST (*35*, *49*)

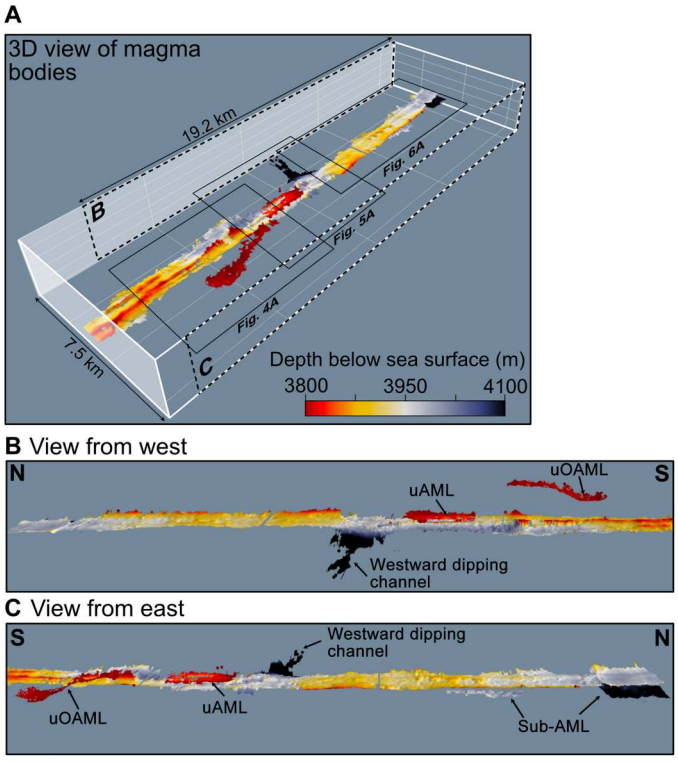

Fig. 3. Perspective view of the magma bodies mapped in the seismic volume from ~9°46.5′ to 9°56.5′N. (**A**) 3D view of AML within a grid to emphasize the morphology of the AML. The southern, central, and northern segments are outlined in black boxes and shown in Figs. 4A, 5A, and 6A, respectively. The black dashed boxes along longer sides of the white grid delimit regions presented as the side views of the shallow magmatic system tilted for ~5° in (**B** and **C**). Important morphological features are indicated: uAML, upper AML. The color scale in (B and C) is the same as in (A). The structural variations in the magma body are enhanced by using OpendTect's *Z*-scaling (i.e., vertical exaggeration) set to 7.

demarked by small structural offsets (~50 m) in its lineation, evident in high-resolution bathymetry (Fig. 5C).

To the south of the obliquely trending AML depression, we map a small, axis-centered, upper-crustal magma body (uAML) ~875 m wide at ~85 to 150 m above the main AML and extending for 2.2 km along the ridge axis (Fig. 5, A and F). The mapped horizon dips toward the south with high reflectivity focused in its northernmost, shallowest part (fig. S7). A narrow linear gap (<200 m), which is vertically aligned with the ridge-like feature in the main AML below and AST above, is also evident in its central part.

Northern magmatic segment

The northern segment is characterized by the absence of a well-developed AST. Instead, two sets of en échelon fissures are present: one dominating the southern half of the segment and located along the crest of the axial high and the other nested on top of a volcanic ridge parallel to and 600 m east of the ridge axis (Fig. 2A) (*26*). Detailed seafloor mapping shows that the eruption of lava in this region took place predominantly along these off-axis fissures (*34*, *35*), but the mechanism leading to this off-axis lava emplacement remains unclear. Our 3D images show that the AML has a dominant concave-upward shape in cross section in this region, with a shallower eastern rim that rises ~75 m above the average depth of the AML beneath the ridge axis (Fig. 6 and fig. S2), which is vertically aligned with the off-axis fissures. Beneath portions of this shallowing AML edge, we observe the presence of narrow reflection patches resembling the signal from the main AML, which we attribute to sub-AML (Figs. 3C and 6A).

About 70 m east of the off-axis fissures, a prominent ridge-parallel fault scarp is present, which served as a dam for the recent eruptions and near which a newly discovered high-temperature vent field has been found (Fig. 6A) (*31*). From the surface expression of the fault and vent fluid chemistry, it was speculated that the fault plane potentially provided the pathway for hydrothermal fluids to penetrate the crust and mine heat from near the AML edge, reaching as deep as ~160 m above the AML edge, to fuel the off-axis high-temperature vent (*31*). Given the proximity of the fault and possible projection at depth to near the AML, it is noteworthy that this structure was not exploited as a magma pathway for the eruption. There is evidence from field exposures of relict volcanic systems that faults can serve as magma pathways [e.g., (*7*, *50*)]. However, the orientation of normal faults relative to the regional stress field is optimized for shear motion and, hence, not ideal for opening pathways for dike propagation (*12*).

DISCUSSION

Connectivity between the AML and Lamont seamount mantle melt anomaly

A long-standing question is why eruptions and hydrothermal venting are focused at the 9°50′N site relative to elsewhere along the well-studied stretch of the EPR from 9° to 10°N given the near-uniform spreading rates and, hence, expectation of similar eruption frequencies. The 9°50′N region is the site of the shallowest ridge axis bathymetry and a broader axial high, which has been attributed to enhanced mantle melt supply (*51*). However, there is no evidence for thicker crust or larger melt volumes in the shallow mantle below (*52*–*55*), as would be expected if this was a long-term locus of higher melt supply. Therefore, it is unclear why this region has been the focus site of multiple eruptions, whereas adjacent regions have not erupted.

Our observations, in conjunction with prior geochemical (*56*) and seafloor morphological studies (*57*), indicate that this localized magmatic robustness results from the interaction of the central magmatic segment with the heterogeneous shallow mantle melt source that has fed the 50-km-long Lamont seamount chain as the spreading-center approaches it, in relation with the northwest drift of the Pacific Plate over the asthenosphere. The youngest of the five well-developed volcanic cones, Sasha seamount, is only 8 km from the ridge axis and located on 0.1–million year–old crust (*56*). Although isotopically and chemically diverse, basalts sampled from these Lamont volcanic cones show dominantly primitive compositions (*56*, *57*), which, along with the absence of evidence for hydrothermal venting, was used to argue that the Lamont seamount magmas have short crustal residence times without formation of magma accumulations (*56*). However, between Sasha seamount and the EPR at about 3 to 7 km from the axis, prior analysis of the 3D seismic dataset revealed two off-axis magma bodies (OAMLs) in the lower crust at a depth of ~3.2 to 4.8 km bsf (*42*). In the high-resolution seafloor horizon mapped in our seismic volume above these OAMLs, we identify a prominent feature with a circular high (~10 m deep and <800 m wide). We

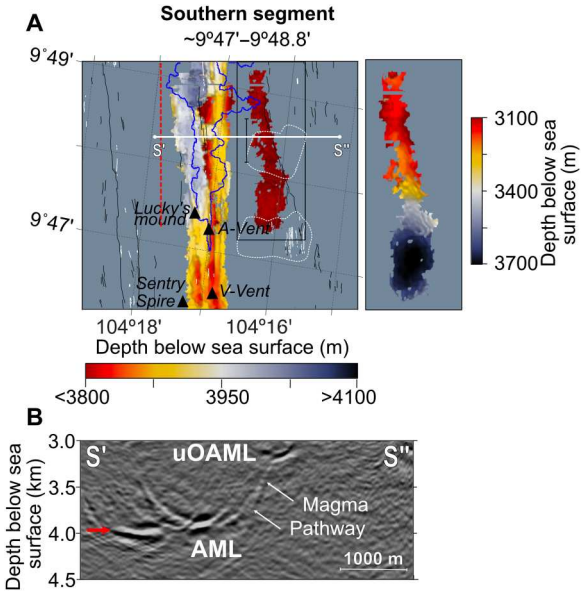

Fig. 4. Magma bodies beneath the southern segment. (**A**) Plan view of the magma body horizons mapped beneath the southern segment, which extends from ~9°47′ to 48.8′N (Fig. 3). The dashed red line marks the western part of the AML that appears as a separate lens. The black box outlines the region around the upper-crust off-axis magma body (uOAML) shown in the subpanel on the right with different color scale to emphasize its topography. The black bar indicates the along-axis extent of the potential magma pathways connecting this magma body with the AML. Dashed white lines show the outline of lower crustal OAMLs (*42*). The thick white line shows the location of the seismic section extracted from the volume shown in (**B**). The red arrow in (B) marks the down-dropped part of the axis-centered AML discussed in text, and the thin white arrows indicate the reflection signal that we interpret as the magma pathway. The remaining elements are as in Fig. 2. (A) without interpretations is in fig. S2B.

interpret it as a nascent caldera that hosts an inflating and constructive dome indicating the birth of a new seamount of the Lamont chain (Fig. 8), the center of that is ~5 km from the ridge axis. On the basis of the spatial alignment of this feature with the Lamont seamounts, we attribute the formation of the nascent caldera to subsurface magma movements associated with the OAMLs. These OAMLs are fed from the shallow mantle source for the Lamont seamount chain (Fig. 7B), inferred from geochemical data to originate at pressures of ~9 to 10 kbar (~30 km) (*56*). The proximity of the OAMLs and nascent caldera with the westwardly dipping magma body imaged beneath the central segment in our data (Figs. 5A, 7B, and 8) strongly suggests that these off-axis crustal accumulations are contributing melt to the on-axis shallow magma body. The oblique trend of the northern half of the central AML segment relative to the ridge axis trend, rotated westward toward the west flank triangular sheet (Fig. 5A), further supports this hypothesis and indicates a rotated stress regime near the depth of the AML in this region. The 8.5° dip of the western sheet and the depth and location of the OAMLs relative to the western edge of the melt channel implies nonvertical pathways for melt delivery. We thus infer that melt migration is taking place along low-angle pathways in the mid-lower crust, governed by the axial thermal structure (Fig. 7B).

The contribution of magma from the OAMLs located beneath the nascent caldera could help explain the variation in the geochemical signature of basaltic glasses collected along the ridge axis (*38*). The average MgO percent composition (8.2/8.5 wt % for the 2005–2006/1991–1992 eruption events, respectively) of lavas from the central segment is consistently higher and close to the average MgO% = 8.2 reported for the Lamont seamounts (*56*). A sample with the highest MgO (wt %) is recovered from the top of a cone on the western edge of the shallower OAML (Fig. 8B). Collectively, the observed geochemical signatures point toward a more primitive and higher temperature magma source than that feeding the adjacent segments where lower MgO% (<8) lavas are sampled (fig. S8). The relatively small but statistically significant (*38*) differences in MgO% across the magmatic segments could be explained by already diluted magma that has undergone fractionation in the OAMLs before being delivered to the central AML segment. Alternatively, smaller volumes of primitive melt may be delivered from the off-axis system directly to the central AML segment, which would still be sufficient to perturb the stresses and lead to an eruption. On the basis of the available data, we cannot distinguish between the two scenarios, as we cannot assess the volume of magma delivered from the off-axis system to the central AML segment.

Several seafloor morphological characteristics also support a genetic connection between the central segment and the Lamont seamount chain. First, the northern edge of the locally shallower and broader ridge axis (~60 m shallower and 3 to 4 km wider) coincides with where the extrapolated trend of the youngest Lamont seamounts intersects the ridge axis and is just north of the northern edge of the westwardly dipping triangular channel (fig. S9). Second, the decrease in size of seamounts along the Lamont chain toward the ridge axis (*57*) is consistent with increased partitioning of magma between the seamounts and the ridge axis with time. On the basis of these combined observations, we infer that the central segment has been consistently oversupplied with magma reaching the shallow-level magmatic system, through localized off-axis feeding to the AML, relative to adjacent ridge segments. Enhanced magma feeding, primarily to the shallow part of the axial magmatic system and not to the deeper part, could account for more frequent eruptions without the creation of thicker crust in this location, thereby addressing a long-standing contradiction.

Illuminating DRZs and constraints on eruption dynamics

Numerous theoretical modeling studies have examined how the shape of magma bodies and stress state and properties of the host rock interact to determine where dikes nucleate and eruptions occur [e.g., (*1*, *4*, *5*, *7*)]. These models typically assume smooth bodies of spherical or ellipsoidal geometry embedded in a purely elastic matrix. Our high-resolution images of the magma source body of an active portion of the MOR volcanic system challenge these models by showing that magma bodies do not have simple smooth geometrical shapes but display prominent elongate fine-scale topography that is vertically aligned with eruptive fissure zones at the seafloor. On the basis of these spatial relationships and the expectation of vertically oriented dikes aligned parallel to the ridge axis in the extensional MOR environment, we interpret this topography as the signatures of DRZs of the last eruption that have been preserved over the 2-year post-eruption period to when our data were acquired.

At both the southern and central segments, the DRZ is located along the approximate center of the AML, while along the northern segment, it is located along the eastern edge of the AML (Figs. 2B,

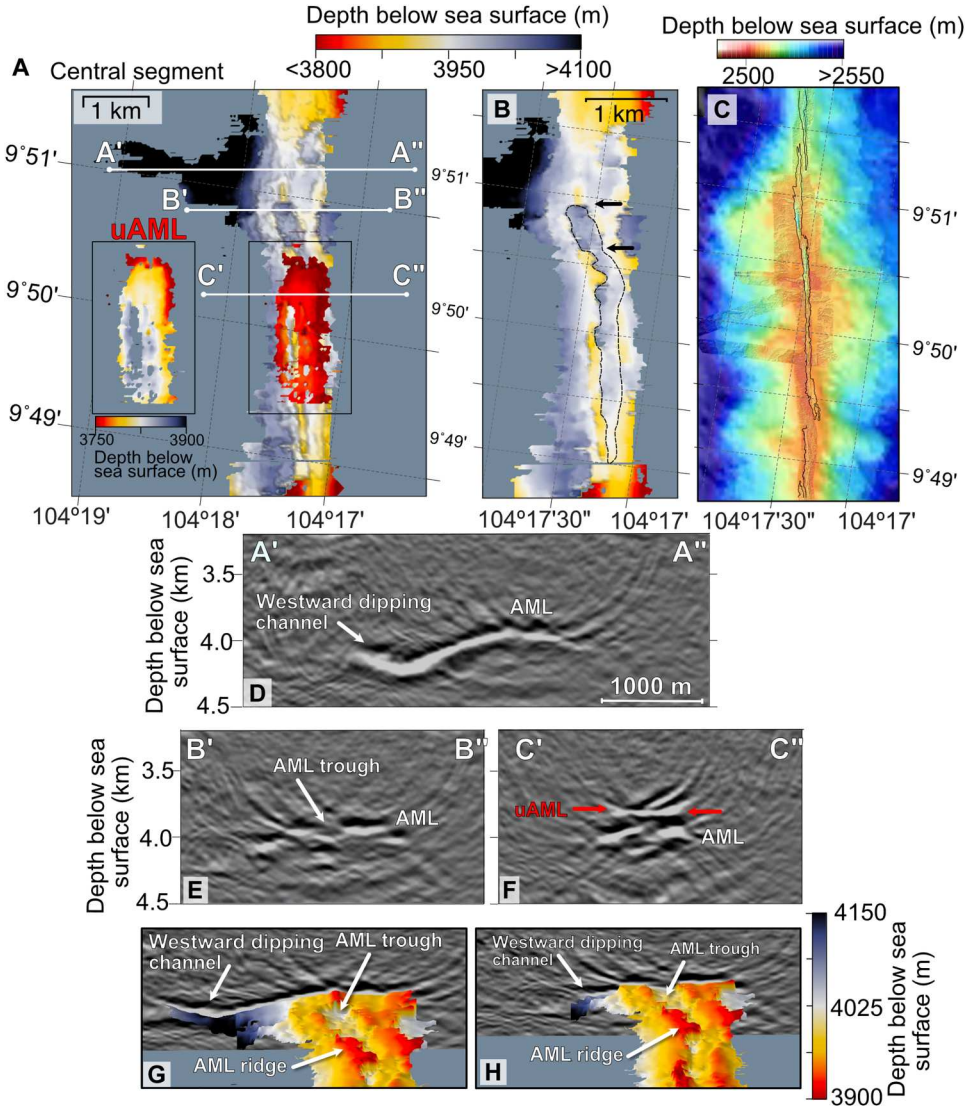

Fig. 5. High-resolution 3D morphology of the magma body beneath the main eruption region. (**A**) Plan view of the AML beneath the central segment extending from 9°48.8′ to 9°51.4′N (Fig. 3). The black box outlines the region around the uAML, shown in the inset in different color scale to emphasize its morphology. The same panel without interpretation superimposed is shown in fig. S2C. Thick white lines indicate locations of seismic sections shown in (D to F). (**B**) Plan view of the AML without the uAML (no scaling is applied). Black dashed line outlines the depression or trough identified in the AML; black arrows delimit the latitudinal extent of the obliquely trending portion of this trough. (**C**) Composite bathymetry data combining resolutions of 30 m (*71*) and 3 m (*70*) is shown. A thin black line outlines the AST (*35*). (**D** to **F**) Seismic sections extracted from the seismic volume to show the variations in the reflection signal originating from the AML, with the most prominent morphological features indicated. The red arrows in (F) mark the reflection from the shallower magma accumulation. The locations of the seismic sections are marked in (A). The panels are at the same horizontal and vertical scale. (**G** and **H**) Perspective 3D view of the AML horizon and intersection with seismic volume to emphasize the morphology of the AML: ridge and trough features and the westward-dipping channel (vertical exaggeration as in Fig. 3).

4A, 5B, and 6A). Furthermore, at the southern and northern segments, a ridge-like/rim feature is present at the DRZ, while along the central segment, a prominent trough bounded by narrow ridges along its eastern and western edges, as well as at its northern limit, is observed. We interpret this trough as an eruption-related excavation of a formerly broad ridge (locally reaching ~500 m in width). Prior studies of melt content in the AML have been conducted using the 2008 along-axis seismic dataset crossing all three segments and include 1D waveform modeling of data from the central segment at 9°49.1′N, as well as partial offset stacking and amplitude variation versus angle of incidence analysis along the 2D profiles (*43*, *44*). Within the extent of the central segment, these seismic lines sample the AML roughly along the trough that we identify in 3D (fig. S7) and indicate the presence of a moderate-to-low melt content. This observation in along-axis lines is consistent with our interpretation of the AML trough representing the zone of melt extraction. The volume of lava erupted in the 2005–2006 episode, which is well constrained from seafloor mapping, has been compared in prior studies to the speculated volume of the magma reservoir to estimate eruption recurrence intervals for this region with predictions that an eruption is imminent in the coming few years (*35*, *43*). These calculations make use of an

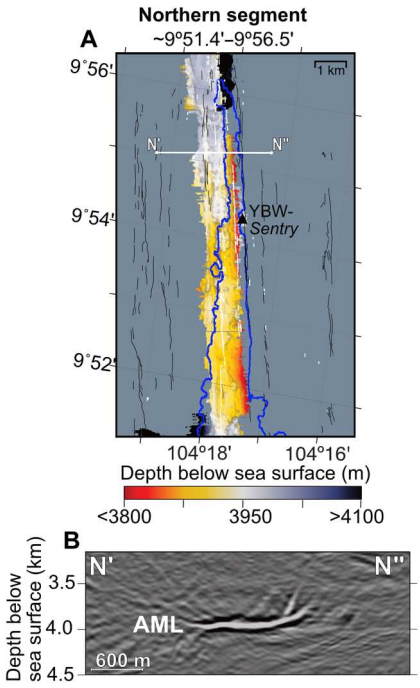

Fig. 6. Magma body beneath the northern segment. (**A**) Plan view of the northern segment AML horizon extending from ~9°51.4′ to 56.5′N (Fig. 3). The triangle marks the location of the newly discovered hydrothermal vent field YBW-Sentry at 9°54.34′N, 104°17.67′W (*31*). The white horizontal line shows the location of the seismic section, extracted from the volume, displayed in (**B**). The remaining elements are as in Fig. 2. (A) without interpretations is shown in fig. S2D.

average AML width (600 m) based on sparse legacy 2D axis-crossing seismic profiles, estimated magma lens thickness (10 to 30 m), and melt content (>70% melt) derived from 1D waveform modeling for the AML outside the eruption zone (at 9°42.8′N) and the assumption that these values are representative of the physical properties of the pre-eruption magma lens across its full width. The obtained seismic images allow for much improved estimates of magma lens volume and indicate the total volume of the three magmatic segments that sourced the recent eruptions was underestimated in these prior studies (table S1).

Furthermore, the observations of a prominent trough beneath the eruptive fissure zone of the central segment indicate that the AML was not uniformly drained during the eruption and provide the best constraints available on the minimum melt volume extracted from this segment during the eruption. On the basis of the trough dimensions and assuming 100% melt content before eruption, we estimate an extracted volume of 42×10^6 m^3, which is about twice the volume of the lava flow erupted from the central segment and plausible dike volume (table S2). The remaining extracted volume is comparable to the estimated volume of the shallow sill found <150 m above the AML along the southern half of the central segment, raising the possibility that this sill was intruded as part of the eruption episode (Fig. 9). The depth of this sill is comparable to estimates of the thickness of the thermal conductive boundary layer (CBL) that separates the AML from the convectively cooling crustal lid (*58*). We speculate that horizontal sill intrusion in this region is due to the presence of a large rheological contrast arising from the sharp thermal gradient zone that defines the top of the CBL (Fig. 9). Future analysis of the microseismicity observations acquired in the region over the 2 years before and spanning the eruption episode (*14*, *33*) could shed light on whether emplacement of this shallow lens occurred in the run-up to or during the eruptions.

In contrast to the central segment, along the southern and northern magmatic segments, a localized melt evacuation zone is not imaged. This observation is consistent with the limited volume of erupted lavas and, hence, low amount of magma mobilized from the southern segment (<4% of the total volume of the magma lens; table S1). At the northern segment, where larger melt volumes erupted, the DRZ zone developed along the eastern edge of the AML with perhaps more continuous magma recharge from deeper magma bodies that are imaged beneath this shallowing edge (Figs. 3C and 7C). Assuming only the magma from the shallow portion of the eastern AML edge was mobilized during the eruption (band centered on shallow ridge ~200 m wide), the obtained volume for a 20-m-thick lens with 71% melt would roughly correspond to the volume of the emplaced lava above the northern segment and intruded 1-m-wide dike.

The lineated AML troughs and shoals that we image along the DRZs for the recent eruptions indicate that magma does not accumulate uniformly within magma lenses nor that it is uniformly extracted; the base level melt content across the volume of a magma body does not simply rise or fall with replenishment and withdrawal. Instead, highly localized and lineated zones of shallower and deeper topography are found. The lineated AML ridges, we image, may evolve from DRZs of previous eruptions that are then maintained as local shoals during inter-eruption periods through both thermal erosion of the host rock (stopping) and magma buoyancy. Through magma buoyancy, the edges of lineated troughs left by evacuation of melt from the magma lens may evolve through time into new AML ridges. Analytical and numerical solutions assuming an elastic rheology predict that failure in the crustal lid leading to dike intrusion will occur preferentially at structural edges and angularities of a pressurized magma body (*59*). Once developed, local relief in the AML will maintain stress concentrations, which, in turn, may lead to more frequent triggering of eruptions at the same location. This view of stress perturbations associated with magma body topography offers a plausible explanation for the observed intense intrusive episodes that occur along the same fissures (e.g., in Iceland) (*60*). Furthermore, remarkable spatial stability of the dike nucleation zone is required to explain the common observation of narrow 1-m-wide dikes with one-sided chilled margins (i.e., dike-in-dike intrusions) in outcrops of oceanic crust (*61*).

Triggering of volcanic eruptions

For volcanic eruptions to occur, magma pressures must be sufficient for magma to reach the surface and erupt, and a magma conduit must develop to connect the magma source to the surface. However, whether conduit nucleation initiates from the bottom, when magma pressures exceed a critical level, propagating upward (i.e., bottom-up), or from the top because of, for example, tectonic stresses exceeding a critical level leading to opening downward (i.e., top-down), is a key question [e.g., (*9*, *15*, *62*)]. In prior studies of MOR eruptions, findings of spatially segmented compositional variations in erupted lavas from an assumed continuous fissure system suggest the top-down opening of the upper crust initiating vertical dike propagation from the

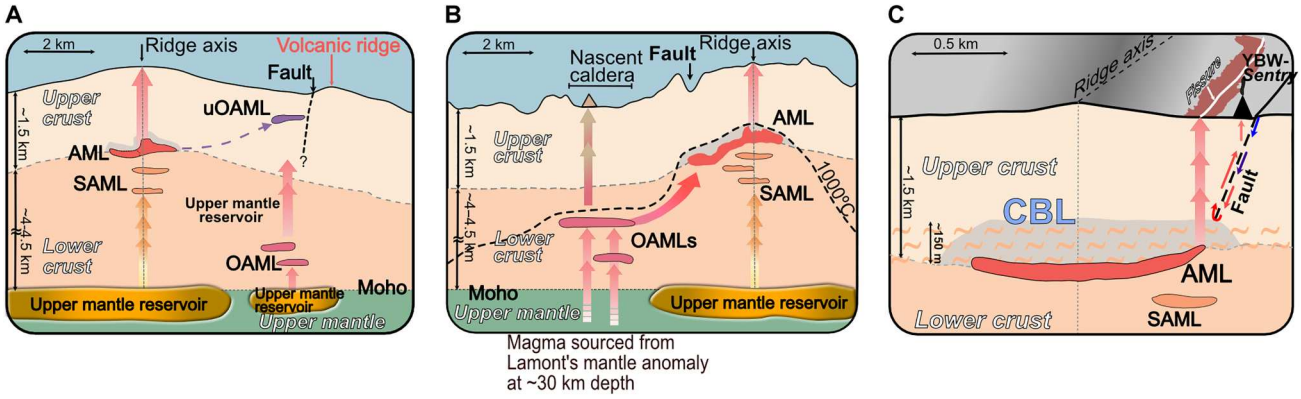

Fig. 7. Schematic profiles illustrating main features of magma plumbing system at each segment of the eruption zone. (**A**) Southern segment: AML with ridge-like feature (vertically exaggerated) underlies the ridge axis. The AML's thermal gradient zone (~700° to 1000°C) is marked in gray area. Away from the ridge axis, an uOAML is present; it is fed by a magma channel from the AML (dashed purple line) and potentially from the lower crust OAMLs (*42*), as indicated by arrows. The eastern edge of the uOAML is inferred to extend to a fault plane (dashed black line). (**B**) Central segment: Lamont mantle melt anomaly feeding the lower crustal OAMLs beneath the nascent caldera, which, in turn, channels magma to the AML, following crustal isotherms (an inferred 1000°C isotherm is shown in dashed line) as indicated by arrows. The gray area shows the AML thermal gradient region. (**C**) Northern segment: Dikes nucleate from the shallow eastern edge of the AML (faded red arrows), and lavas erupt from a mapped system of fissures vertically above, marked in white. The nearby fault (solid black line on the seafloor) and its inferred plane in depth (dashed line) is suggested to be a down flow zone for hydrothermal fluids marked in colored arrows ranging from blue to red to indicate temperature variation from cold to hot (*31*), respectively. The bottom of a convecting hydrothermal fluid cell (~400°C) is marked in gray area. The region with an orange pattern marks the dike-gabbro transition zone. The remaining elements are as in Fig. 1. The illustrations are not drawn to scale. The representations of the magma bodies and seafloor are highly vertically exaggerated; approximative vertical and horizontal scales for the upper and lower crust are provided in all panels and for the AML thermal gradient zone in (C).

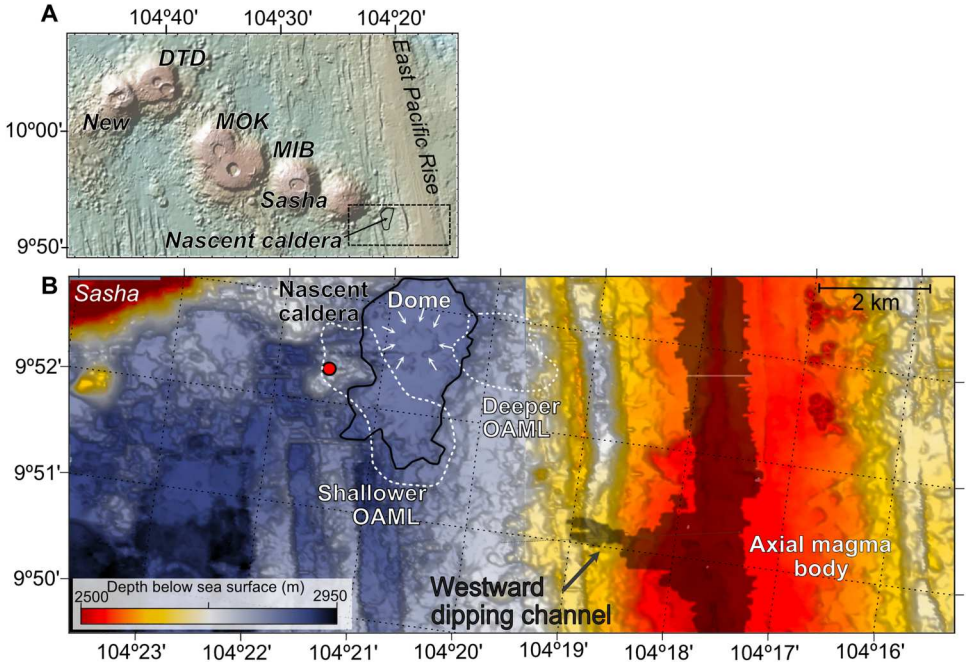

Fig. 8. Lamont seamount chain interaction with the EPR. (**A**) Bathymetry map from GeoMapApp of the Lamont seamount chain with seamounts marked by names and the location of the nascent caldera outlined in thin black line. The dashed box indicates the location of the panel shown in (B). (**B**) High-resolution seafloor horizon mapped in 3D seismic data, revealing a constructional, dome feature (marked in white arrows) in the nascent seamount caldera, outlined in black line. The red circle represents the location of the sample with MgO (wt %) = 9.44 recovered from top of the cone near the nascent caldera at 9°52.3′N/104°21.5′W (*57*). Previously mapped off-axis magma body OAMLs (*42*) are outlined in white dashed lines: The shallower one is at 3.2 km, and the deeper one is at 4.8 km bsf. A shaded silhouette of the AML horizon is superimposed at the ridge axis with the westward dipping channel marked.

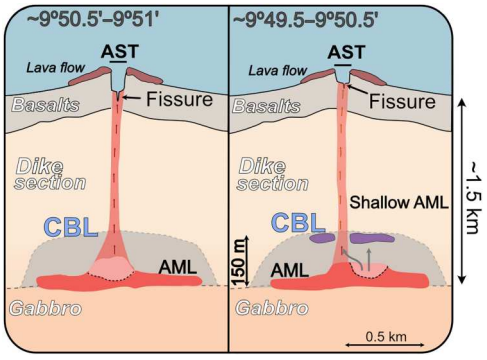

Fig. 9. Schematic view of the two cross sections illustrating the diking episode during the last documented eruption within the central segment The cartoon on the left depicts the region of the northern, obliquely trending part of the trough where the main diking event was recorded by microseismicity (fig. S10) (*14*). The magma conduit develops from a DRZ and connects vertically with the surface at deep AST (fig. S6C). The cartoon on the right portrays the mobilization of magma from the remaining part of the trough and horizontal emplacement of the uAML. The magma conduit develops at the western rim of the DRZ to connect with the surface at the AST. One part of thus mobilized magma is emplaced as the uAML within the upper crust at the top of the CBL. The light red areas underlined by black dashed lines represent the surface of the regions excavated by the eruption, as seen in our snapshot from 2008 (Fig. 5A). The illustrations are not to scale; approximate vertical and horizontal scales are provided as guidance.

underlying heterogeneous magma body [e.g., (*16*–*20*)]. However, ovepressurization of magma bodies by injection of hotter and more primitive magma is typically evoked in convergent and intraplate settings [e.g., (*38*, *63*)].

While these processes are not mutually exclusive, our observations combined with other eruption characteristics indicate that magmatic overpressure and stress conditions near the AML likely play the primary role in dike nucleation and eruption triggering at the EPR 9°50′N site, which could be considered as an end-member case for the EPR eruptions. From petrologic studies of erupted lavas, it was inferred that the central segment was replenished with primitive melt only 6 weeks or less before the eruption and that this magma replenishment event likely contributed to triggering the eruption (*64*). Our observations suggest the melt replenishment event was associated with melt delivery from the Lamont seamount source along the west flank triangular sheet. Microseismicity monitoring studies found that the earliest seismicity of the primary eruption event on 26 January 2006, was focused within this same region of the oblique trending AML, indicating dike initiation in this region (*14*; fig. S10). Across the three AML segments that erupted, driving magma pressures inferred from estimates of lava effusion rates are highest for the central segment where lavas also travelled the farthest (*65*). Magma ascent rates estimated from the seismicity observations are also highest for the central segment (*14*), which is consistent with higher magma pressures at this segment. That DRZ troughs in the AML surface are only present at the central segment is also consistent with higher magma pressures that allowed for greater evacuation of melt from the AML in this region.

On the basis of local earthquake observations of near concurrent eruption from all three magmatic segments under different magma pressures conditions, as well as the spatiotemporal sequence of seismic events preceding the January 2006 eruption, it was previously proposed that this eruption was triggered primarily from the top-down because of tectonic stresses in the crustal lid exceeding a critical level (*14*). In contrast, our observations support dike initiation at the central segment, likely via magma replenishment event from the west flank Lamont seamount source that led to magma overpressures in the AML. Stress perturbations associated with dike initiation at this segment then triggered dike nucleation along the adjoining segments focused along the shallow ridge-like DRZs in the AML topography formed during prior eruptions where both locally higher magma pressures and volcano edifice stress concentrations are expected. How top-down opening would coincidentally localize to the eastern edge of the northern segment AML, 0.6 km away from the morphologic ridge axis, but at the AML center along the southern and central segments is difficult to envision. AML topography likely played the key role in focusing dike nucleation and conduit opening to the seafloor above. Bottom-up triggering of eruptions at the central 9°50′N segment may represent an end-member case for EPR eruptions given the role of magma delivery to this segment from an off-axis magma source. However, the findings of lineated topographic highs along the AML segments of the eruption zone, which likely develop over the inter-eruption period into sites of higher magma pressure via buoyancy-driven melt migration, suggest that a component of bottom-up triggering via magma overpressures could contribute to EPR eruptions more generally.

In these interpretations, we assume that our 2-year post eruption seismic images retain a signature of the pre-eruption morphology of the shallow magma bodies. To confirm these inferences, new repeat seismic studies to support 4D time-lapse imaging will be required. Important questions regarding how the geometry and extent of the AML segments and their DRZ structures evolve over a volcanic cycle (e.g., over what time scales does DRZ topography evolve, do DRZ troughs disappear, do DRZ ridges grow, and how ephemeral are shallow upper crustal sills) are unknown. Our results, which indicate that detailed magma body morphology plays a key role in dike nucleation and eruption triggering in the EPR 9°N region also bear on volcanic hazard studies in subaerial settings, which are of high societal interest for global populations. Considering the geometry of shallow magma accumulations sculpted by volcanism in next-generation numerical models would allow for a more realistic depiction of volcano dynamics and eruption localization and improved volcanic hazard assessment and mitigation.

MATERIALS AND METHODS

Data acquisition

Data were collected in Summer 2008 aboard *R/V Marcus G. Langseth* during the MGL0812 3D seismic survey. To acquire the data, four 6-km-long solid streamers, each with 468 hydrophones spaced at 12.5 m, were deployed at 7.5 m below sea surface. To optimize the time for data collection, race track acquisition geometry was adopted, with three race track loops (fig. S1). The final box was completed with reshot and infill lines. For all lines, the distance between the cables was set to 150 m, which resulted in a 262.5-m-wide swath, with eight common-midpoint lines, at each pass of the ship. Well-tuned, two-array seismic sources with 3300-in^3 total volume firing in alternating mode were used to produce acoustic energy at 37.5-m

space interval. The maximum recorded time was ~10 s, and the sampling rate was 2 ms.

Seismic data processing

We apply a standard processing flow to the 2008 EPR 9°50′N data volume before migration. It included the definition of 3D geometry, noise removal, spherical divergence correction, surface-consistent amplitude correction, resampling to 4 ms, data filtering (≤100 Hz), and application of spectral boost of the data to flatten the spectrum and enhance low frequencies (2 to 5 Hz) (*46*). To migrate the 3D seismic volume, we use a standard 3D Kirchhoff prestack depth migration scheme (*66*). Initial migration tests using water velocity (*67*) were focused on the seafloor, encompassing the entire area sampled by the seismic data (30 km by 40 km). For instance, this test volume was used to map the seafloor horizon in the vicinity of the Lamont seamounts and reveal the nascent caldera (Fig. 8B).

For the final prestack depth migration, which includes seafloor and AML reflectors, we use the published 3D *P*-wave velocity model (*39*) obtained from the advanced 3D elastic FWI approach (*46*). We must mention that the 3D elastic FWI code used for defining the migration velocity model does not include anisotropy and attenuation. In addition, the FWI work was focused on exploiting primarily the signal at source-receiver offsets >2 km and waveforms originating from the upper crust (first 800 m) (*39*), where velocity variations are the highest. As the FWI window was extending from 0 to 5 s, some of the events at mid to far source-receiver offset were modeled and helped update the initial velocities for the remaining part of the upper crust. To date, this velocity model represents the best-available velocity model for the upper crust in the EPR eruption site, and we use it as such. To reduce the computational cost of 3D prestack depth migration, we defined a subvolume. In the along-axis direction, it includes racetracks 1 and 2 and the northernmost part of racetrack 3 (fig. S1). In the cross-axis direction, it is ridge axis centered with a total width of 7 km to ensure adequate migration aperture for the AML. In two-way travel time, we limit the volume to 5 s. In addition, we limit the migration to near-offsets (<1.5 km) to avoid artifacts from the triplication originating from the high vertical velocity gradient present in the upper crust. After performing 3D prestack depth migration (bin size, 25 m by 25 m) using the best-available velocity model, we stack the data to produce a seismic data cube. Last, we run several rounds of interactive residual velocity corrections applied directly to the volume and visually inspected to improve the imaging and reduce as much as possible some of the locally present migration smiles. The ensemble of seismic data processing, including the residual velocity corrections, was done using the algorithms proprietary to Shell International Global Solution.

Horizon extraction

Seismic horizons were picked using OpendTect, an open-source tool. Both the seafloor and AML horizons were picked in autotrack mode using the seed trace method. In both cases, we picked the negative polarity event as the most prominent and continuous phase of the mapped reflection events. The optimal size of the search window used is ±10 m for the seafloor and ±25 m for the AML. The size of the search window for each horizon were defined after visually inspecting results of tests varying the window size from ±5 to ±50 m conducted using a built-in tool. In addition, we used the built-in correlation option, with windows ranging between −50 and 50 m and 85% of correlation threshold to better constrain the picking parameters. The picks were filtered applying a built-in median filter using one inline/crossline filter step and gridded with preservation of holes ≥50 m. In this study, we show the data from 9°46′ to 9°56.5′N (fig. S1). We need to emphasize that, here, we focus only on mapping strong reflection events of high confidence. For lower confidence events where we could not readily discriminate whether the event was real or artifact (diffractions or contamination from far offsets), we omit the pick and leave it for further detailed examination (fig. S11). We interpret the ridge-ward dipping events at 9°48′ to 48.5′N as potential magma pathways because, in depth slice, we observe a consistent linear feature that cannot be mistaken for diffraction hyperbola (fig. S12). In our interpretations, we focus primarily on relative variation in depth of the AML reflectors, as the superposition of depth uncertainties associated with picking (5 to 20 m), filtering (~20 m), and the velocity model (challenging to evaluate because of the ill-posed and nonlinear nature of the elastic FWI code used) affect the absolute depth values that are difficult to quantify.

Energy attribute

In OpendTect, the energy attribute is computed "as the squared sum of the sample values in the specified time-gate divided by the number of samples in the gate" (*68*). Here, we use a depth gate of ±35 m centered on the AML horizon. The energy attribute, with values always >0, provides a measure of the reflectivity of the AML horizon. In the interpretation, we use the energy attribute as a proxy for relative variation in melt content, such that the zones with high values in energy attribute indicate AML regions with potentially higher melt content. The assumption is that the variation in amplitude originates entirely from the variation of melt versus crystal content and is not affected by thin-bed tuning effects.

Volume estimates

Pre-eruption magma volume

Polygon tool, a built-in function in OpendTect software, was used to obtain the surface area of the AML segments. These values, rounded to the first decimal point, were used to estimate the volume of each AML segment for an assumed thickness range of 10 to 30 m (*43*). The same approach was used to define the volume of the westward dipping channel and the uOAML. For the central segment, to the pre-eruption volume estimate, we also include the volume of the remanent AML ridge-like feature, assuming that the thickness of this ridge above the main AML surface corresponds to its average height (57 m). For comparison with estimates from the previous study using 1D waveform modeling (*43*), we also calculate melt volumes assuming 71% melt content in the AML. The results are presented in table S1. The table includes the volumes of the lava emplaced on the seafloor from a recent study (*35*).

Eruption evacuated magma volume

The Polygon tool was also used to define the surface area of the AML trough found along the central segment, which we interpret as the result of magma evacuation from this magma lens during the eruption. Trough melt volume is obtained using an average depth of 47 m, assuming 100% melt content. The volume of the uAML is estimated from its surface area for a lens thickness range of 10 to 30 m. Last, the volume of the intruded dikes was obtained assuming 1-m-wide dikes (*69*), latitudinal extent of the AML trough (3700 m),

and average depth of the central AML segment (1515 m). The results are presented in table S2.

Supplementary Materials

This PDF file includes:

Figs. S1 to S12
Tables S1 and S2

REFERENCES AND NOTES

1. A. Tibaldi, Structure of volcano plumbing systems: A review of multi-parametric effects. *J. Volcanol. Geotherm. Res.* **298**, 85–135 (2015).
2. K. V. Cashman, R. S. J. Sparks, J. D. Blundy, Vertically extensive and unstable magmatic systems: A unified view of igneous processes. *Science* **355**, eaag3055 (2017).
3. R. S. J. Sparks, C. Annen, J. D. Blundy, K. V. Cashman, A. C. Rust, M. D. Jackson, Formation and dynamics of magma reservoirs. *Phil. Trans. R. Soc. A* **377**, 20180019 (2019).
4. E. Rivalta, F. Corbi, L. Passarelli, V. Acocella, T. Davis, M. T. De Vito, Stress inversions to forecast magma pathways and eruptive vent location. *Sci. Adv.* **5**, eaau9784 (2019).
5. L. Caricchi, M. Townsend, E. Rivalta, A. Namiki, The build-up and triggers of volcanic eruptions. *Nat. Rev. Earth Environ.* **2**, 458–476 (2021).
6. K. Jaxybulatov, N. M. Shapiro, I. Koulakov, A. Mordret, M. Landès, C. Sens-Schönfelder, A large magmatic sill complex beneath the Toba caldera. *Science* **346**, 617–619 (2014).
7. A. Gudmundsson, Magma chambers: Formation, local stresses, excess pressures, and compartments. *J. Volcanol. Geotherm. Res.* **237-238**, 19–41 (2012).
8. S. M. Carbotte, A. Arnulf, M. Spiegelman, M. Lee, A. Harding, G. Kent, J. P. Canales, M. Nedimović, Stacked sills forming a deep melt-mush feeder conduit beneath Axial Seamount. *Geology* **48**, 693–697 (2020).
9. D. C. Roman, K. V. Cashman, Top–down precursory volcanic seismicity: Implications for 'Stealth' magma ascent and long-term eruption forecasting. *Front. Earth Sci.* **6**, 1–18 (2018).
10. R. Scandone, K. V. Cashman, S. D. Malone, Magma supply, magma ascent and the style of volcanic eruptions. *Earth Planet. Sci. Lett.* **253**, 513–529 (2007).
11. S. M. Carbotte, M. Marjanović, A. F. Arnulf, M. R. Nedimović, J. P. Canales, G. M. Arnoux, Stacked magma lenses beneath mid-ocean ridges: Insights from new seismic observations and synthesis with prior geophysical and geologic findings. *J. Geophys. Res. Solid Earth* **126**, e2020JB021434 (2021).
12. E. Rivalta, B. Taisne, A. P. Bunger, R. F. Katz, A review of mechanical models of dike propagation: Schools of thought, results and future directions. *Tectonophysics* **638**, 1–42 (2015).
13. P. McLeod, S. Tait, The growth of dykes from magma chambers. *J. Volcanol. Geotherm. Res.* **92**, 231–245 (1999).
14. Y. J. Tan, M. Tolstoy, F. Waldhauser, W. S. Wilcock, Dynamics of a seafloor-spreading episode at the East Pacific Rise. *Nature* **540**, 261–265 (2016).
15. T. Girona, F. Costa, G. Schubert, Degassing during quiescence as a trigger of magma ascent and volcanic eruptions. *Sci. Rep.* **5**, 18212 (2015).
16. K. H. Rubin, M. C. Smith, E. C. Bergmanis, M. R. Perfit, J. M. Sinton, R. Batiza, Geochemical heterogeneity within mid-ocean ridge lava flows: Insights into eruption, emplacement and global variations in magma generation. *Earth Planet. Sci. Lett.* **188**, 349–367 (2001).
17. K. H. Rubin, J. M. Sinton, Inferences on mid-ocean ridge thermal and magmatic structure from MORB compositions. *Earth Planet. Sci. Lett.* **260**, 257–276 (2007).
18. K. H. Rubin, J. M. Sinton, J. Maclennan, E. Hellebrand, Magmatic filtering of mantle compositions at mid-ocean ridge volcanoes. *Nat. Geosci.* **2**, 321–328 (2009).
19. D. A. Clague, J. B. Paduan, B. M. Dreyer, W. W. Chadwick, K. R. Rubin, M. R. Perfit, A. T. Fundis, Chemical variations in the 1998, 2011, and 2015 lava flows from axial seamount, Juan de Fuca Ridge: Cooling during ascent, lateral transport, and flow. *Geochem. Geophys. Geosyst.* **19**, 2915–2933 (2018).
20. E. C. Bergmanis, J. M. Sinton, K. H. Rubin, Recent eruptive history and magma reservoir dynamics on the Southern East Pacific Rise at 17°30′S. *Geochem. Geophys. Geosyst.* **8**, 10.1029/2007GC001742, (2007).
21. K. H. Rubin, A. Soule, W. W. Chadwick, D. J. Fornari, D. A. Clague, R. W. Embley, E. T. Baker, M. R. Perfit, D. W. Caress, R. . P. Dziak, Volcanic eruptions in the deep sea. *Oceanography* **25**, 142–157 (2012).
22. M. Marjanović, S. M. Carbotte, H. Carton, M. R. Nedimović, J. C. Mutter, J. P. Canales, A multi-sill magma plumbing system beneath the axis of the East Pacific Rise. *Nat. Geosci.* **7**, 825–829 (2014).
23. S. M. Carbotte, M. Marjanović, H. Carton, J. C. Mutter, J. P. Canales, M. R. Nedimović, S. Han, M. R. Perfit, Fine-scale segmentation of the crustal magma reservoir beneath the East Pacific Rise. *Nat. Geosci.* **6**, 866–870 (2013).
24. E. E. E. Hooft, R. S. Detrick, G. M. Kent, Seismic structure and indicators of magma budget along the Southern East Pacific Rise. *J. Geophys. Res.* **102**, 27319–27340 (1997).
25. G. M. Kent, A. J. Harding, J. A. Orcutt, Distribution of magma beneath the East Pacific Rise between the Clipperton Transform and the 9°17′N Deval from forward modeling of common depth point data. *J. Geophys. Res.* **98**, 13945–13969 (1993).
26. G. M. Kent, S. C. Singh, A. J. Harding, M. C. Sinha, J. A. Orcutt, P. J. Barton, R. S. White, S. Bazin, R. W. Hobbs, C. H. Tong, J. W. Pye, Evidence from three-dimensional seismic reflectivity images for enhanced melt supply beneath mid-ocean -ridge discontinuities. *Nature* **406**, 614–618 (2000).
27. S. C. Singh, G. M. Kent, J. Collier, A. J. Harding, J. A. Orcutt, Melt to mush variations in crustal magma properties along the ridge crest at the southern East Pacific Rise. *Nature* **394**, 874–878 (1998).
28. R. A. Dunn, D. R. Toomey, S. C. Solomon, Three-dimensional seismic structure and physical properties of the crust and shallow mantle beneath the East Pacific Rise at 9°30′N. *J. Geophys. Res.* **105**, 23537–23555 (2000).
29. R. A. Dunn, A dual-level magmatic system beneath the East Pacific Rise, 9°N. *Geophys. Res. Lett.* **49**, e2022GL097732 (2022).
30. K.L. Von Damm, Evolution of the hydrothermal system at East Pacific Rise 9°500N: Geochemical evidence for changes in the upper oceanic crust, in *Hydrothermal Interactions between the Lithosphere and Oceans*, C. R. German, J. Lin, L. M. Parson, Eds. (Geophysical Monograph Series, American Geophysical Union, 2004), vol. 148, pp. 285–305.
31. J. M. McDermott, R. Parnell-Turner, T. Barreyre, S. Herrera, C. C. Downing, N. C. Pittoors, K. Pehr, S. A. Vohsen, W. S. Dowd, J.-N. Wu, M. Marjanović, D. J. Fornari, Discovery of active off-axis hydrothermal vents at 9° 54′N East Pacific Rise. *Proc. Natl. Acad. Sci. U.S.A.* **119**, e2205602119 (2022).
32. R. M. Haymon, D. J. Fornari, K. L. Von Damm, M. D. Lilley, M. R. Perfit, J. M. Edmond, W. C. Shanks III, R. A. Lutz, J. M. Grebmeier, S. Carbotte, D. Wright, E. McLaughlin, M. Smith, N. Beedle, E. Olson, Volcanic eruption of the mid-ocean ridge along the East Pacific Rise crest at 9°45–52′N: Direct submersible observations of seafloor phenomena associated with an eruption event in April, 1991. *Earth Planet. Sci. Lett.* **119**, 85–101 (1993).
33. M. Tolstoy, J. P. Cowen, E. T. Baker, D. J. Fornari, K. H. Rubin, T. M. Shank, F. Waldhauser, D. R. Bohnenstiehl, D. W. Forsyth, R. C. Holmes, B. Love, M. R. Perfit, R. T. Weekly, S. A. Soule, B. Glazer, A seafloor spreading event captured by seismometers. *Science* **314**, 1920–1922 (2006).
34. S. A. Soule, D. J. Fornari, M. R. Perfit, K. H. Rubin, New insights into mid-ocean ridge volcanic processes from the 2005–2006 eruption of the East Pacific Rise, 9°46′N–9°56′N. *Geology* **35**, 1079–1082 (2007).
35. J.-N. Wu, R. Parnell-Turner, D. J. Fornari, G. Kurras, N. Berrios-Rivera, T. Barreyre, J. M. McDermott, Extent and volume of lava flows erupted at 9°50′N, East Pacific Rise in 2005–2006 from autonomous underwater vehicle surveys. *Geochem. Geophys. Geosyst.* **23**, e2021GC010213 (2022).
36. J.-N. Wu, R. Parnell-Turner, D. J. Fornari, N. Berrios-Rivera, T. Barreyre, J. M. McDermott, The role of on- and off-axis faults and fissures during eruption cycles and crustal accretion at 9° 50′N, East Pacific Rise. *Geochem. Geophys. Geosyst.* **24**, e2022GC010794 (2023).
37. J. Escartín, S. A. Soule, D. J. Fornari, M. A. Tivey, H. Schouten, M. R. Perfit, Interplay between faults and lava flows in construction of the upper oceanic crust: The East Pacific Rise crest 9° 25′-9°58′N. *Geochem. Geophys. Geosyst.* **8**, 10.1029/2006GC001399, (2007).
38. A. R. Goss, M. R. Perfit, W. I. Ridley, K. H. Rubin, G. D. Kamenov, S. A. Soule, S. A. Fundis, D. J. Fornari, Geochemistry of lavas from the 2005–2006 eruption at the East Pacific Rise, 9° 46′N-9°56′N: Implications for ridge crest plumbing and decadal changes in magma chamber compositions. *Geochem. Geophys. Geosyst.* **11**, 10.1029/2009GC002977, (2010).
39. M. Marjanović, R.-É. Plessix, A. Stopin, S. C. Singh, Elastic versus acoustic 3-D full waveform inversion at the East Pacific Rise 9°50′N. *Geophys. J. Int.* **216**, 1497–1506 (2019).
40. M. Marjanović, S. M. Carbotte, H. D. Carton, M. R. Nedimović, J. P. Canales, J. C. Mutter, Crustal magmatic system beneath the East Pacific Rise (8°20′ to 10°10′ N): Implications for tectono-magmatic segmentation and melt transport at fast-spreading ridges. *Geochem. Geophys. Geosyst.* **19**, 4584–4611 (2018).
41. J. P. Canales, H. D. Carton, S. M. Carbotte, J. C. Mutter, M. R. Nedimović, M. Xu, O. Aghaei, M. Marjanović, K. Newman, Network of off-axis melt bodies at the East Pacific Rise. *Nat. Geosci.* **5**, 279–283 (2012).
42. O. Aghaei, M. R. Nedimović, M. Marjanović, S. M. Carbotte, J. P. Canales, H. Carton, N. Nikić, Constraints on melt content of off-axis magma lenses at the East Pacific Rise from analysis of 3-D seismic amplitude variation with angle of incidence. *J. Geophys. Res. Solid Earth* **122**, 4123–4142 (2017).
43. M. Xu, J. P. Canales, S. M. Carbotte, S. M. H. Carton, M. R. Nedimović, J. C. Mutter, Variations in axial magma lens properties along the East Pacific Rise (9°30′–10°00′N) from swath 3D

seismic imaging and 1D waveform inversion. *J. Geophys. Res. Solid Earth* **119**, 2721–2744 (2014).
44. M. Marjanović, H. D. Carton, M. R. Nedimović, S. M. Carbotte, J. C. Mutter, J. P. Canales, Distribution of melt along the East Pacific Rise from 9°30′ to 10°N from an amplitude variation with angle of incidence (AVA) technique. *Geophys. J. Int.* **203**, 1–21 (2015).
45. S. Han, S. M. Carbotte, H. Carton, J. C. Mutter, O. Aghaei, M. R. Nedimović, J. P. Canales, Architecture of on- and off-axis magma bodies at EPR 9°37–40′N and implications for oceanic crustal accretion. *Earth Planet. Sci. Lett.* **390**, 31–44 (2014).
46. R.-É. Plessix, P. Milcik, H. Rynja, A. Stopin, K. Matson, S. Abri, Multiparameter full-waveform inversion: Marine and land examples. *Lead. Edge* **32**, 1030–1038 (2013).
47. A. F. Arnulf, A. J. Harding, G. M. Kent, S. M. Carbotte, J. P. Canales, N. R. Nedimović, Anatomy of an active submarine volcano. *Geology* **42**, 655–658 (2014).
48. Y. Zha, S. C. Webb, S. L. Nooner, W. C. Crawford, Spatial distribution and temporal evolution of crustal melt distribution beneath the East Pacific Rise at 9°–10°N inferred from 3-D seafloor compliance modeling. *J. Geophys. Res. Solid Earth* **119**, 4517–4537 (2014).
49. D. J. Fornari, M. Tivey, S. Hans, M. Perfit, D. Yoerger, A. Bradley, M. Edwards, R. Haymon, D. Scheirer, K. Von Damm, T. Shank, A. Soule, Submarine lava flow emplacement at the East Pacific Rise 9° 50′N: Implications for uppermost ocean crust stratigraphy and hydrothermal fluid circulation, in *Thermal Structure of the Ocean Crust and the Dynamics of Hydrothermal Circulation* (AGU Geophysical Monograph, American Geophysical Union, 2013), vol. 148, pp. 187–217 .
50. K. Thomson, Determining magma flow in sills, dykes and laccoliths and their implications for sill emplacement mechanisms. *Bull. Volcanol.* **70**, 183–201 (2007).
51. D. S. Scheirer, K. C. Macdonald, Variation in cross-sectional area of the axial ridge along the East Pacific Rise: Evidence for the magmatic budget of a fast spreading center. *J. Geophys. Res. Solid Earth* **98**, 7871–7885 (1993).
52. G. A. Barth, J. C. Mutter, Variability in oceanic crustal thickness and structure: Multichannel seismic reflection results from the northern East Pacific Rise. *J. Geophys. Res.* **101**, 17951–17975 (1996).
53. O. Aghaei, M. R. Nedimović, H. D. Carton, S. M. Carbotte, J. P. Canales, J. C. Mutter, Crustal thickness and Moho character of the fast-spreading East Pacific Rise from 9°42′N to 9°57′N from poststack-migrated 3-D MCS data. *Geochem. Geophys. Geosyst.* **15**, 634–657 (2014).
54. B. Boulahanis, S. M. Carbotte, P. J. Huybers, M. R. Nedimović, O. Aghaei, J. P. Canales, C. H. Langmuir, Do sea level variations influence mid-ocean ridge magma supply? A test using crustal thickness and bathymetry data from the East Pacific Rise. *Earth Planet. Sci. Lett.* **535**, 116121 (2020).
55. D. R. Toomey, D. Jousselin, R. A. Dunn, W. S. D. Wilcock, R. S. Detrick, Skew of mantle upwelling beneath the East Pacific Rise governs segmentation. *Nature* **446**, 409–414 (2007).
56. J. F. Allan, R. Batiza, M. R. Perfit, D. J. Fornari, R. O. Sack, Petrology of Lavas from the Lamont Seamount Chain and adjacent East Pacific Rise, 10° N. *J. Petrol.* **30**, 1245–1298 (1989).
57. D. J. Fornari, M. R. Perfit, J. F. Allan, R. Batiza, R. Haymon, A. A. Barone, B. F. R. William, T. Smith, T. Simkin, M. A. Luckman, Geochemical and structural studies of the Lamont seamounts: Seamounts as indicators of mantle processes. *Earth and Planet. Sci. Lett.* **89**, 63–83 (1988).
58. S. C. Singh, J. S. Collier, A. J. . Harding, G. M. Kent, J. A. Orcutt, Seismic evidence for a hydrothermal layer above the solid roof of the axial magma chamber at the southern East Pacific Rise. *Geology* **27**, 219–222 (1999).
59. E. Cañón- Tapia, Volcanic eruption triggers: A hierarchical classification. *Earth Sci. Rev.* **129**, 100–119 (2014).
60. T. Thordarson, G. Larsen, Volcanism in Iceland in historical time: Volcano types, eruption styles and eruptive history. *J. Geodyn.* **43**, 118–152 (2007).
61. A. Nicolas, F. Boudier, J. Koepke, L. France, B. Ildefonse, C. Mevel, Root zone of the sheeted dike complex in the Oman ophiolite. *Geochem. Geophys. Geosyst.* **9**, Q05001 (2008).
62. B. Voight, A. T. Linde, I. S. Sacks, G. S. Mattioli, R. S. J. Sparks, D. Elsworth, D. Hidayat, P. E. Malin, E. Shalev, C. Widiwijayanti, S. R. Young, V. Bass, A. Clarke, P. Dunkley, W. Johnston, N. McWhorter, J. Neuberg, P. Williams, Unprecedented pressure increase in deep magma reservoir triggered by lava-dome collapse. *Geophys. Res. Lett.* **33**, L03312 (2006).
63. M. O. Garcia, A. Pietruszka, J. M. Rhodes, K. Swanson, Magmatic processes during the prolonged Pu'u 'O'o eruption of Kilauea Volcano, Hawaii. *J. Petrol.* **41**, 967–990 (2000).
64. A. Moore, L. A. Coogan, F. Costa, M. R. Perfit, Primitive melt replenishment and crystal-mush disaggregation in the weeks preceding the 2005–2006 eruption 9°50′N, EPR. *Earth Planet. Sci. Lett.* **403**, 15–26 (2014).
65. A. T. Fundis, S. A. Soule, D. J. Fornari, M. R. Perfit, Paving the seafloor: Volcanic emplacement processes during the 2005–2006 eruptions at the fast spreading East Pacific Rise, 9°50′N. *Geochem. Geophys. Geosyst.* **11**, Q08024 (2010).
66. O. Yilmaz, *Seismic Data Analysis: Processing, Inversion, and Interpretation of Seismic Data* (Society of Exploration Geophysicists, 2001).
67. E. E. Vera, J. C. Mutter, P. Buhl, J. A. Orcutt, A. J. Harding, M. E. Kappus, R. S. Detrick, T. M. Brocher, The structure of 0- to 0.2-m.y.- old oceanic crust at 9°N on the East Pacific Rise from expanded spread profiles. *J. Geophys. Res. Solid Earth* **95**, 15529–15556 (1990).
68. dGB Earth Sciences, OpendTect Pro and Plugins User Documentation v6.6, Chapter 1.4, Thalweg Tracker (2021). [accessed on 22 October 2022].
69. R. Qin, W. R. Buck, Why meter-wide dikes at oceanic spreading centers? *Earth Planet. Sci. Lett.* **265**, 466–474 (2008).
70. V. Ferrini, Processed ship-based Multibeam Sonar Data (version 2) from the East Pacific Rise (EPR) Spreading Center at Segment 9°N acquired during the Atlantis expedition AT18–12, IEDA (2011).
71. S. M. White, R. M. Haymon, S. M. Carbotte, A new view of ridge segmentation and near-axis volcanism at the East Pacific Rise, 8–12°N, from EM300 multibeam bathymetry. *Geochem. Geophys. Geosyst.* **7**, 10.1029/2006GC001407, (2006).

Acknowledgments: We thank the *R/V Langseth*'s captain, crew, and technical staff who participated during the 2008 data collection. Furthermore, we are grateful to R. A. Weissel (LDEO) and S. Reker (Shell) for transferring the raw seismic data to Shell's powerful cluster in Houston, which enabled the timely completion of velocity modeling and data processing using proprietary codes/software. We gratefully acknowledge the help of C. Haneveld in data migration. The fruitful discussions with R. W. Buck, R. Parnell-Turner, J.-n. Wu, D. J. Fornari, K. Rubin, L. France, and F. Waldhauser were invaluable in building the interpretation. The assemble of bathymetry grids, outlining the AST, and the geometry of the seafloor and AML horizons were examined using ArcMap, which was also used for conversions between the global (UTM/degree) and local (inline/crossline) coordinate systems. The interpretation and analyses of seismic data were made in OpendTect. For producing figures, we used Generic Mapping Tools (GMT), GeoMapApp, MATLAB, OpendTect, and Affinity Design. **Funding:** This study was partially supported by Marie S. Curie Individual Fellowship awarded to Milena Marjanović (proposal no: 655283 3DWISE; 2015-2017), with the secondment at Shell Global Solutions International B.V. in the Netherlands. Funding for acquisition of the data used in this study was from NSF grant no. 0327872 awarded to S.M.C. and J.C.M. **Author contributions:** Milena Marjanović and S.M.C. interpreted the data and wrote the paper with contributions from all coauthors A.S., S.C.S., R.-É.P., Miloš Marjanović, M.R.N., J.P.C., H.D.C., J.C.M., and J.E. Milena Marjanović and A.S. conducted seismic data processing. Milena Marjanović did the velocity modeling with supervision from R.-É.P. and A.S.. Data analyses in OpendTect and ArcMap 10.2 were done by Milena Marjanović and Miloš Marjanović, respectively. The following authors participated in data collection: Milena Marjanović, S.M.C., M.R.N., J.P.C., H.D.C., and J.C.M. **Competing interests:** The authors declare that they have no competing interests. **Data and materials availability:** All data needed to evaluate the conclusions in the paper are present in the paper and/or the Supplementary Materials. The raw seismic data are available at www.marine-geo.org/tools/search/Files.php?data_set_uid=14654. The velocity model obtained using elastic 3D full-waveform inversion can be found at www.marine-geo.org/tools/files/31329. The interpreted AML horizon picks are at www.marine-geo.org/tools/files/31330. All the above data are archived under MGDS.

Submitted 14 April 2023
Accepted 29 August 2023
Published 29 September 2023
10.1126/sciadv.adi2698

ScienceAdvances

Insights into dike nucleation and eruption dynamics from high-resolution seismic imaging of magmatic system at the East Pacific Rise

Milena Marjanovi#, Suzanne M. Carbotte, Alexandre Stopin, Satish C. Singh, René-Édouard Plessix, Miloš Marjanovi#, Mladen R. Nedimovi#, Juan Pablo Canales, Hélène D. Carton, John C. Mutter, and Javier Escartín

Sci. Adv. **9** (39), eadi2698. DOI: 10.1126/sciadv.adi2698